Supporting Information

Local Polarization Strategy for Efficient Sacrificial-free Hydrogen Peroxide Photoproduction

*Donghui Wang, Jin-Gang-Lu Tao, Hai yang Zhang, Po Zhang and Feng Chen**

1. Experimental section

1.1 Materials

1,3,5-triformylphloroglucinol (Tp), 2,4-diamino-1,3,5-triazine (Tz), 4,6-diaminopyrimidine (Da), 2,4-diaminopyridine (Py), and m-phenylenediamine (Ma) were purchased from Bide Pharmatech Co., Ltd. 1,4-Dioxane , mesitylene, acetic acid, N,N-dimethylformamide (DMF) , methanol, Nafion (5 wt%), sodium sulfate (Na_2SO_4), potassium hydrogen phthalate, potassium iodide (KI), sodium iodate ($NaIO_3$), EDTA disodium salt (EDTA-2Na), nitroblue tetrazolium (NBT), silver nitrate ($AgNO_3$), and tert-butanol (tBA) were obtained from Sinopharm Chemical Reagent Co., Ltd. DMPO was supplied by Dojindo Chemical Technology Co., Ltd. All aqueous solutions used in the experiments were prepared using ultrapure water (18.2MΩ·cm).

1.2 Synthesis of COFs

The COFs were synthesized via a one-pot procedure by Schiff base reaction with Tp and four diamines (Tz, Da, Py, and Ma) as the precursors. Typically, 0.2 mmol Tp and 0.3 mmol diamines were added into a Schlenk tube. Then, 1.5 mL mesitylene, 1.5 mL 1,4-Dioxane, and 0.3 mL 6 M AcOH mixture solution was added into the Schlenk tube, which was degassed by three freeze-pump-thaw cycles. The tube was sealed and heated at 120 °C for 72 h. The precipitate was collected by centrifugation and washed with DMF, H_2O and MeOH to remove unreacted precursors and oligomers. Finally, TpTz, TpDa, TpPy, and TpMa were obtained after being dried at 60 °C overnight.

1.3 Material characterization

X-ray diffraction (XRD) data were measured on Bruker D2 Phaser X-ray diffractometer (λ = 0.154 nm). The lattice patterns and morphology of the samples were observed using a transmission electron microscope (TEM, Talos F200X) and a scanning electron microscope

(SEM, Helios G4 UC). Fourier-transform infrared (FTIR) spectra were recorded on a Nicolet 380 infrared spectrometer in the range of 4000-400 cm^{-1}. The solid-state ^{13}C nuclear magnetic resonance (SSNMR) spectra were recorded on Bruker AVANCE NEO 500 M spectrometer. The contents of C and N elements were detected using element analyzer (EA, Elementar Vario EL). The absorbance of I_3^- solution was measured using a Shimadzu ultraviolet-visible spectrophotometer (UV-2600) and diffuse reflectance spectroscopy (DRS) was performed in the range of 200 to 800 nm with $BaSO_4$ as the reference. X-ray photoelectron spectroscopy (XPS) was conducted using a Thermo Fisher ESCALAB 250Xi instrument with Al K*α* excitation source, and internal calibration was performed using the C1*s* binding energy (BE) from carbon contaminants at 284.8 eV. Photoluminescence (PL) were monitored using a fluorescence spectrometer (Edinburgh Instruments FLS980). Thermogravimetric (TG) analysis was performed on a TA Discovery 5500 instrument. Electron paramagnetic resonance (EPR) measurements were carried out on an EPR spectrometer (Bruker BioSpin GmbH) using DMPO as a radical capture reagent. The Brunauer-Emmett-Teller (BET) surface area and pore structure were analyzed by 3FLEX 3500. The in-situ DRIFTS were recorded on Bruker VERTEX 80v.

1.4 Photocatalytic tests

The catalyst (3 mg) was introduced into a 50 mL quartz reactor, followed by the addition of pure water (30 mL) to achieve homogeneous dispersion of the catalyst via 5 min of ultrasonication. Subsequently, the dispersion was saturated with O_2 under dark conditions through continuous injection of O_2 (50 mL min^{-1}) for 30 min. The reaction mixture was then subjected to irradiation under a Xe lamp (CEL-LAX) with sustained O_2 purging for photocatalytic evaluation. Throughout the experiment, the solution was maintained under magnetic agitation at 1200 rpm. Aliquots (1.5 mL) were sampled at 30-min intervals, with photocatalyst removal accomplished via centrifugal filtration.

The amount of H_2O_2 was determined using the iodine titration method. A solution of 1.0 ml 0.4 mol L^{-1} potassium iodide (KI) and 1.0 ml 0.1 mol L^{-1} potassium hydrogen phthalate ($KC_8H_5O_4$) was added to 1.0 ml of the H_2O_2 sample solution, and the solution was allowed to stand for 30 min. H_2O_2 reacted with I^- under acidic conditions to form I_3^- ($H_2O_2 + 3I^- + 2H^+ \rightarrow I_3^- + 2H_2O$), which exhibited strong absorption at around 350 nm[1]. The content of I_3^- was determined by

measuring the absorbance at 350 nm using ultraviolet-visible spectrophotometry. This allowed for the calculation of the total amount of H_2O_2 generated during the reaction.

1.5 Apparent quantum yield measurement

The apparent quantum yield (AQY) produced by H_2O_2 was tested using filters with center wavelengths of 400 nm, 450 nm, 500 nm, 550 nm, and 600 nm. The concentration of photocatalyst in the reaction solution was 0.33 g L^{-1}. The irradiation area was controlled at 0.385 cm^2, and the light intensity was measured using an optical densitometer. The AQY was calculated using the following formula:

$$\eta = \frac{N_e}{N_p} \times 100\% = \frac{2 \times M \times N_A \times h \times c}{S \times P \times t \times \lambda} \times 100\%$$

Where, M represents the number of H_2O_2 molecules produced, N_A is Avogadro's constant, h is Planck's constant, c is the speed of light, S is the irradiation area, P is the irradiation light intensity, t is the duration of the light reaction, and λ is the wavelength of the incident monochromatic light.

1.6 SCC efficiency (%) measurement

The SCC efficiency (%) was evaluated under AM 1.5 G light illumination according to the following equation:

$$\text{SCC efficiency (\%)} = \frac{\left[\Delta G \text{ for } H_2O_2 \text{ generation } \left(\text{J mol}^{-1}\right)\right]\left[H_2O_2 \text{ formed (mol)}\right]}{\left[\text{total input energy (W)}\right]\left[\text{reaction time (s)}\right]} \times 100$$

The free energy (ΔG) for H_2O_2 generation is 117 kJ mol^{-1}.

The H_2O_2 generation rate is $1.72*10^{-5}$ mol per hour, with an irradiated area of 0.385 cm^2 and a light intensity of 270 mW cm^{-2} as measured by a photodensitometer. Substituting these values into the formula yields an SCC efficiency of 0.54%.

1.7 (Photo)electrochemical measurement

Transient photocurrent (*I-T*) and electrochemical impedance spectroscopy (EIS) measurements were conducted on a CHI760E electrochemical workstation (Shanghai CH Instruments Co., Ltd.) equipped with a standard three-electrode system. Ag/AgCl electrode (saturated KCl), platinum foil electrode, and indium tin oxide (ITO) glass electrode (1.0*2.0 cm) were used as reference electrode, counter electrode, and working electrode, respectively. The

preparation process of the working electrode is as follows: 2.0 mg of the prepared catalyst was dispersed in a mixture solution of ethanol (95 μL), water (95 μL), and Nafion (10 μL) by ultrasonication. Then, 100 μL of the suspension was drop-casted onto the ITO electrode, controlling the electrode area to be 1 cm^2. After natural cooling, the electrode was dried under an infrared lamp for 5 minutes. A xenon lamp (300 W, CEL-PF300-T8) was used as the light source, and $NaSO_4$ (0.20 M) was used as the electrolyte. Under open-circuit voltage, photocurrent was collected every 20 s Electrochemical impedance spectroscopy was performed at a DC voltage of -0.5 V (vs. Ag/AgCl), with an AC voltage amplitude of 5 mV and a frequency range from 100 kHz to 0.01 Hz.

The transfer electron number (*n*) and H_2O_2 selectivity of the samples in the ORR reaction were measured using a rotating ring-disk electrode (RRDE) setup[2, 3]. The electrochemical measurements were conducted in a three-electrode system with RRDE as the working electrode, Ag/AgCl as the reference electrode, and a platinum ring as the counter electrode. A phosphate buffer solution (0.1 m pH = 6.9) saturated with O_2 was used as the electrolyte. The RRDE rotation speed was set to 2500 rpm, and the potential range was set from -1.0 to 0.5 V (vs. Ag/AgCl) with a scan rate of 10 mV/s. Prior to electrochemical performance testing, the working electrode was cyclic voltammetry (CV) scanned at a scan rate of 50 mV/s until the curve stabilized. The catalyst ink on the RRDE working electrode was prepared as follows: A total of 5 mg of the sample was combined with 0.5 mL of ethanol, 0.5 mL of water, and 50 μL of Nafion solution, and the resulting mixture was ultrasonicated for 20 min to achieve a homogeneous dispersion. Subsequently, 10 μL of this uniform dispersion was drop-cast onto a clean glassy carbon electrode and allowed to air-dry at room temperature prior to testing.

The number of transferred electrons was calculated according to the following equation:

$$n = 4 \times \frac{I_d}{I_d + I_r/N}$$

The selectivity was determined by the following equation:

$$\%(H_2O_2) = 200 \times \frac{I_r/N}{I_d + I_r/N}$$

Where I_d is the disk current, I_r is the ring current, and N is the collection efficiency (0.37).

1.8 Probing WOR and ORR with low-concentration electron acceptor

To further probe the relationship between WOR and ORR, we adopted a quantitative strategy using a low concentration of Ag^+ (0.1 mM) as an electron acceptor under O_2-free conditions, following previously reported approaches [4]. In this configuration, photogenerated electrons are initially consumed by Ag^+ reduction, while holes drive water oxidation to produce O_2. Once Ag^+ is depleted, the O_2 generated from WOR can subsequently participate in ORR to form H_2O_2. Thus, the amount of H_2O_2 produced can be correlated with the O_2 generated via WOR.

The quantification principle is described as follows. We made the following assumptions:

(1) all added Ag^+ (4n mol) is completely consumed to provide holes that generate the initial O_2 (n mol);

(2) the COFs then reduce O_2 (n mol) to form H_2O_2 (n mol) while simultaneously oxidizing H_2O (n mol) to generate fresh O_2 (1/2 n mol);

(3) the O_2 generated in step (2) continues to participate in H_2O_2 production and WOR, generating additional O_2 (1/4 n, 1/8 n, 1/16 n … mol) until all O_2 is consumed.

Accordingly, the amount of H_2O_2 produced from the initially generated O_2 can be calculated as:

$$n_{H_2O_2} = \sum_{k=1}^{x} n_{O_2} r^{k-1} = \frac{n_{O_2}(1 - r^x)}{1 - r}$$

where $n_{H_2O_2}$ is the generated amount of H_2O_2, n_{O_2} is the amount of generated O_2 by Ag^+, r is 1/2, k is number of reaction cycles for simultaneous H_2O_2 production and WOR. If the initial O_2 generated by Ag^+ (k = 1) was all consumed for H_2O_2 production (i.e., k equals to∞), the total amount of H_2O_2 produced would be 2 times the amount of O_2 (k = 1) and 1/2 times the amount of added Ag^+.

1.9 In-situ Diffuse Reflectance Infrared Fourier Transform Spectra (DRIFTS) Analysis

The sample was placed in in-situ cell. H_2O vapors and O_2 were introduced in the cell. After the sample reached an adsorption-desorption equilibrium within 30 min, the DRIFTS were test under the visible light irradiation.

2. Computational details

First-principles DFT calculations were performed using the Vienna ab initio simulation package

(VASP) [5, 6]and the projector augmented wave (PAW) method [7]. The exchange- correlation effects were treated in generalized gradient approximation (GGA) with the Perdew-Burke-Ernzerhof (PBE) potential [8]. The kinetic energy cutoff was chosen to be 500 eV. The electronic energy was considered self-consistent when the energy change was smaller than 10^{-6} eV. A geometry optimization was considered convergent when the force change was smaller than 0.02 eV/Å. Grimme's DFT-D3 methodology was used to describe the dispersion interactions [9]. The adsorption energy (E_{ads}) was defined as:

$$E_{ads} = E_{ad/sub} - E_{ad} - E_{sub}$$

where $E_{ad/sub}$, E_{ad}, and E_{sub} are the total energies of the optimized adsorbate/substrate system, the adsorbate in the gas phase, and the clean substrate, respectively.

The free energy (G) for elemental reaction step were calculated as:

$$G = E + ZPE - TS + H(T)$$

where E is the total energy calculated by DFT, ZPE is the zero point energy, T is the temperature (298.15 K), S represents the entropy, and $H(T)$ means enthalpy [1]. The zero energy and entropy of the adsorbed substance are calculated based on the frequency of vibration. The free energy of H_2O and H_2 is calculated from the gas phase H_2O at 0.035 bar and H_2 at 298.15 K at 1 bar. The free energy of O_2 is calculated using the following equation:

$$G(O_2) = G(H_2O) - 2G(H_2) + 4.92\text{eV}.$$

Time-dependent density functional theory (TD-DFT) calculations were performed using the B3LYP/6-311G(d) method and basis set with the ORCA program.[10] Analysis and visualization of hole and electron distribution were performed by Multiwfn [11] based on an efficient algorithm and filled with colors using VMD [12].

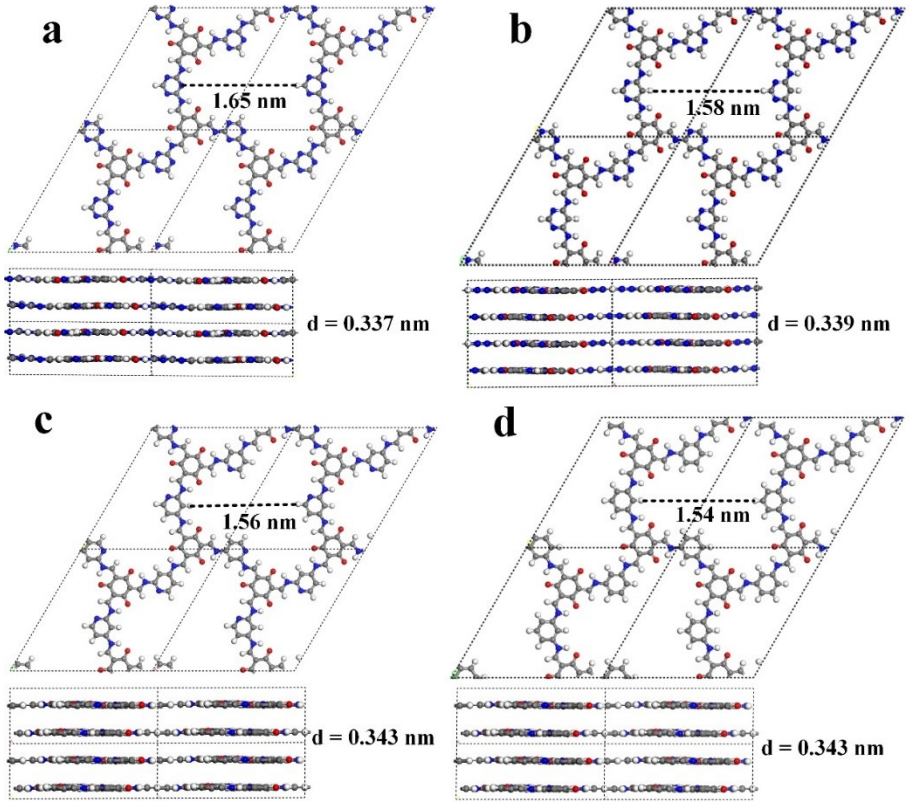

Figure S1. Stacking model structures of COFs. AA stacking model structures of (a) TpTz, (b) TpDa, (c) TpPy, and (d) TpMa from the top and side views.

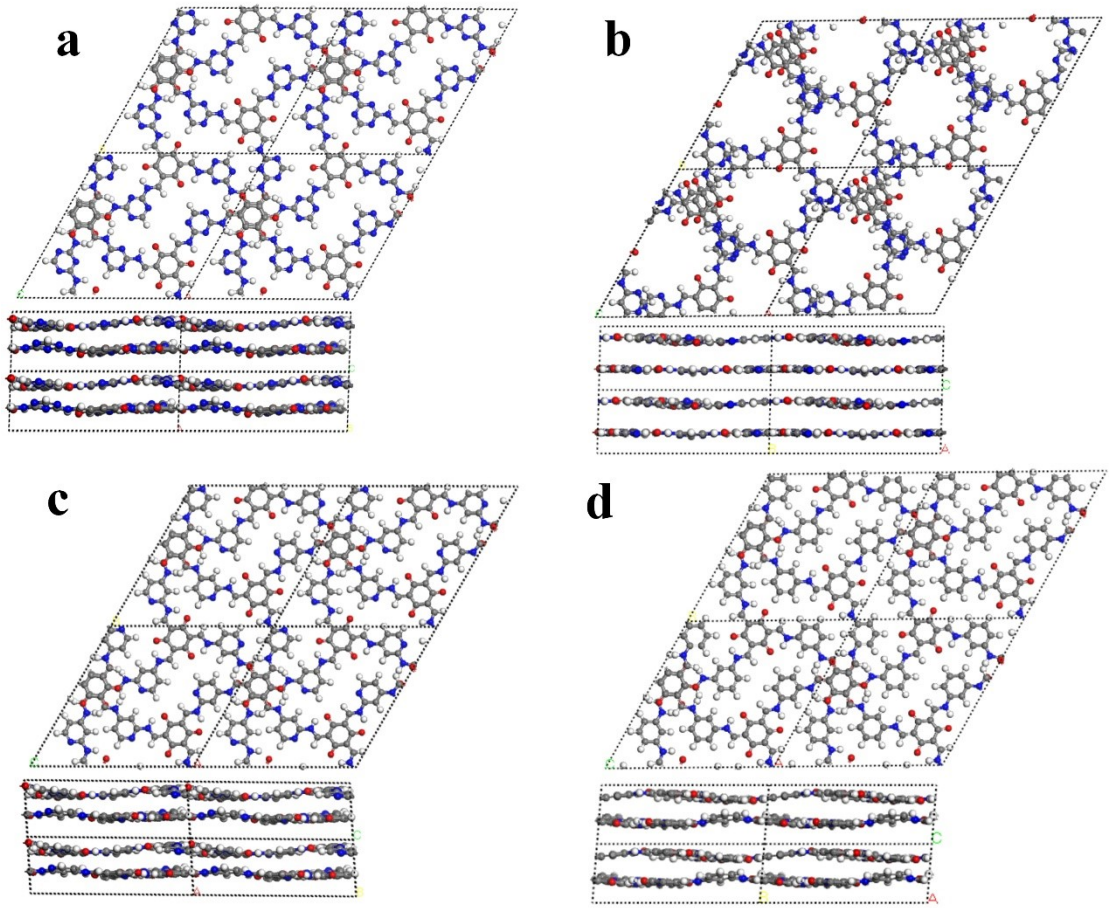

Figure S2. Stacking model structures of COFs. AB stacking model structures of (a) TpTz, (b) TpDa, (c) TpPy, and (d) TpMa from the top and side views.

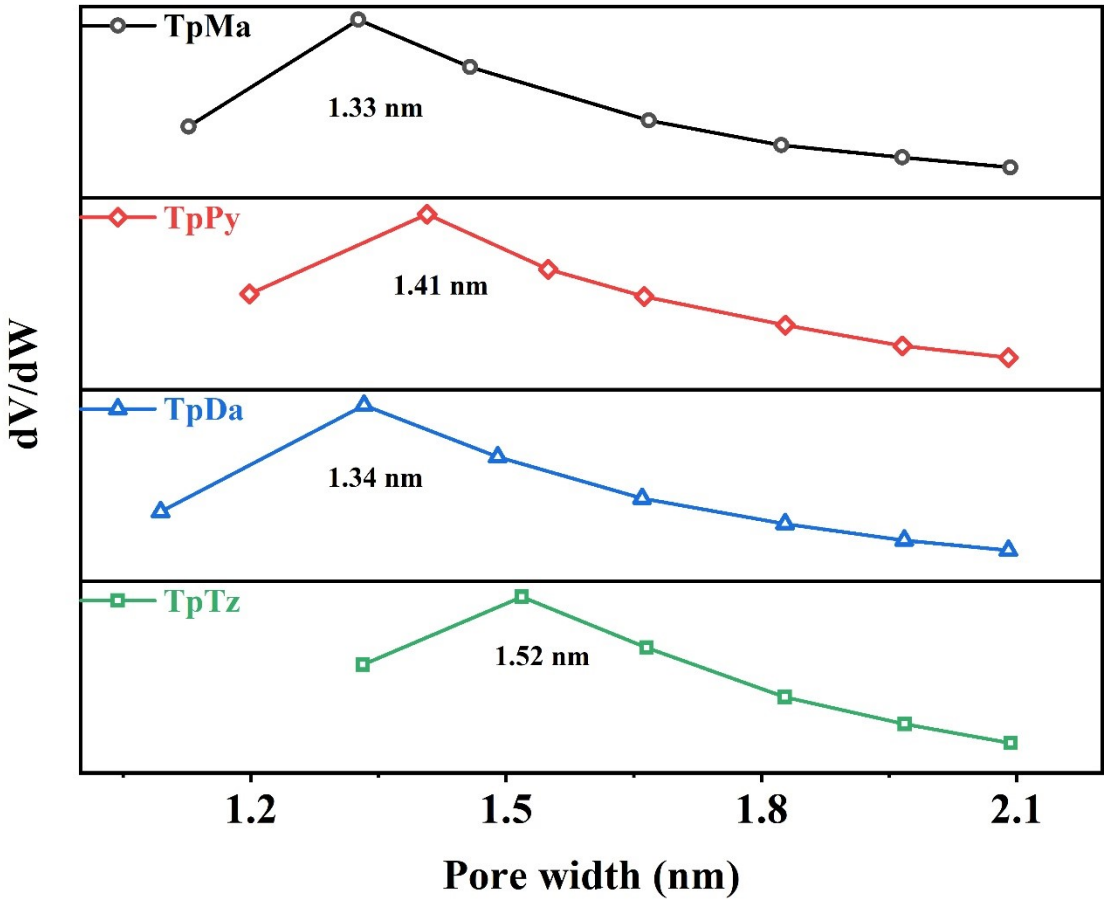

Figure S3. Pore size distributions of COFs.

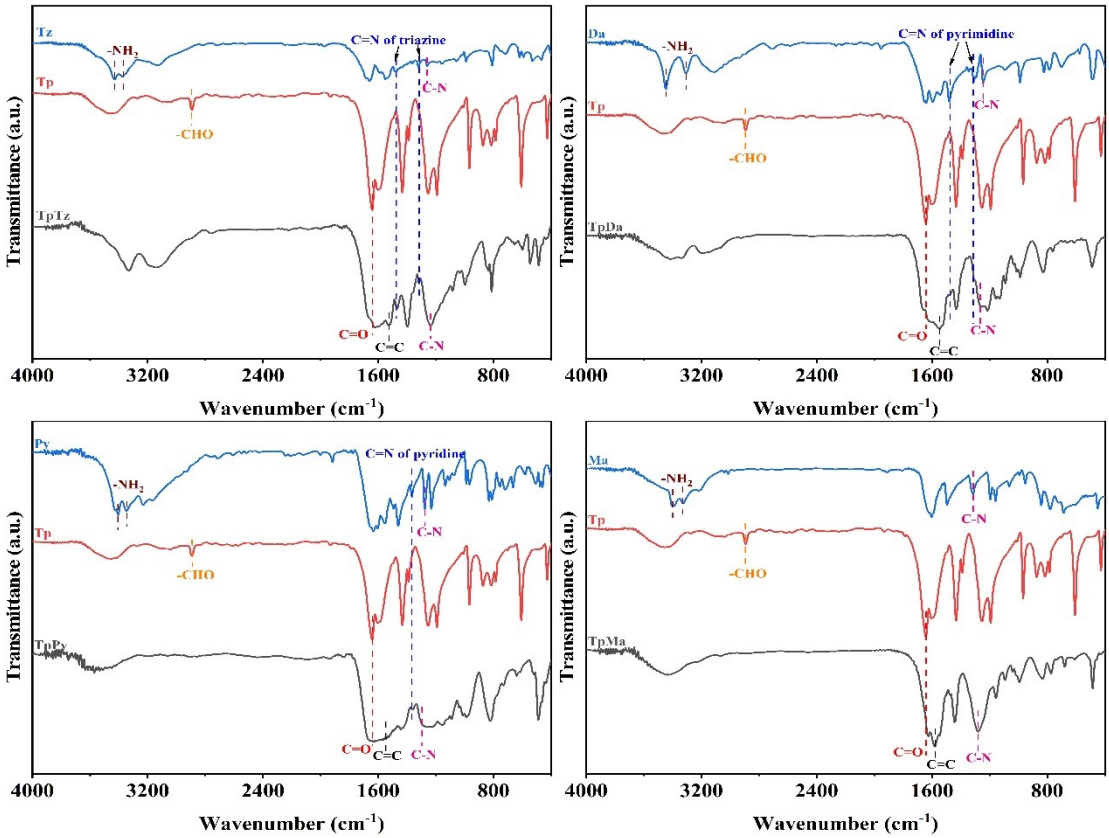

Figure S4. Fourier transform infrared (FT-IR) spectroscopy for Tp, diamine and COFs.

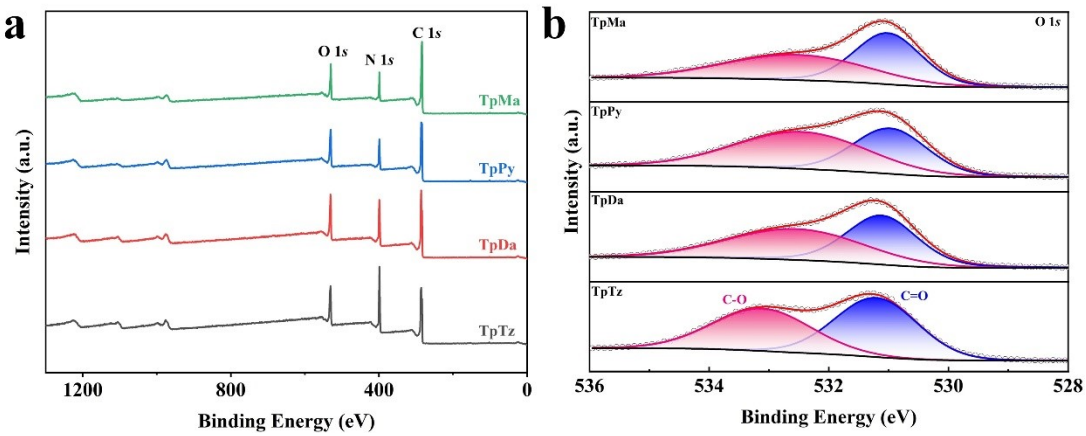

Figure S5. (a)XPS surveys of COFs. (b) O 1s XPS spectra of COFs.

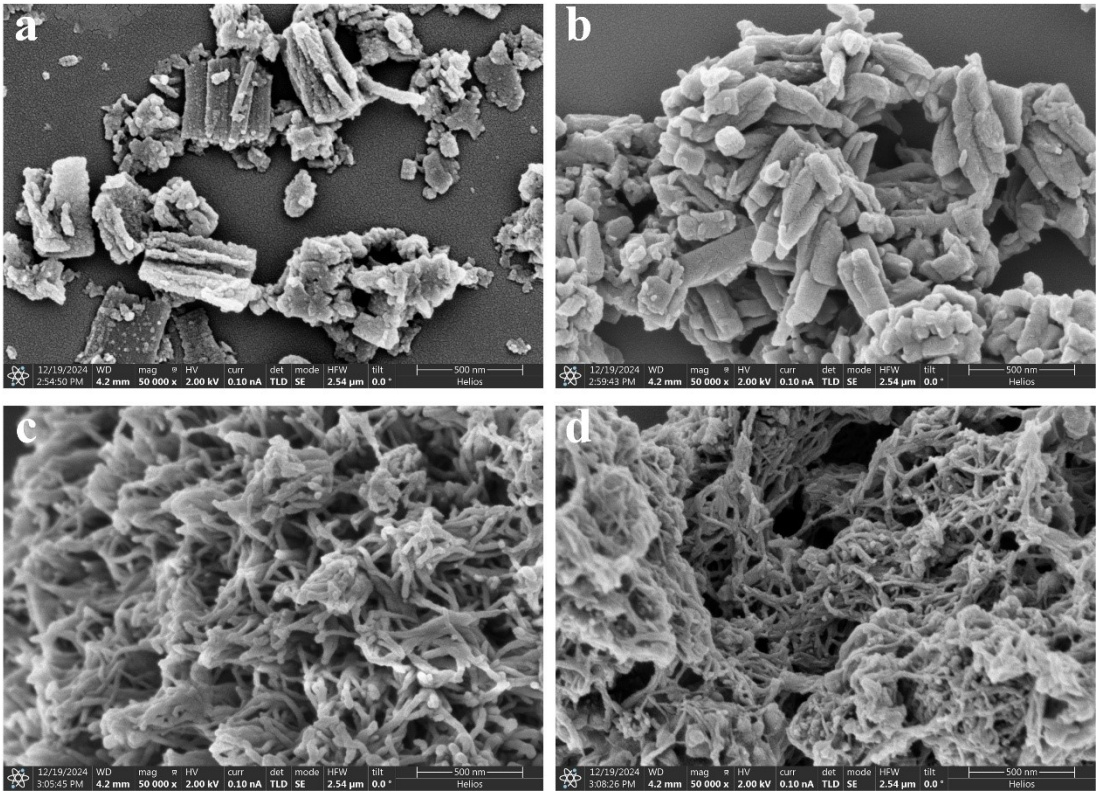

Figure S6. SEM images of (a) TpTz, (b) TpDa, (c) TpPy and (d) TpMa.

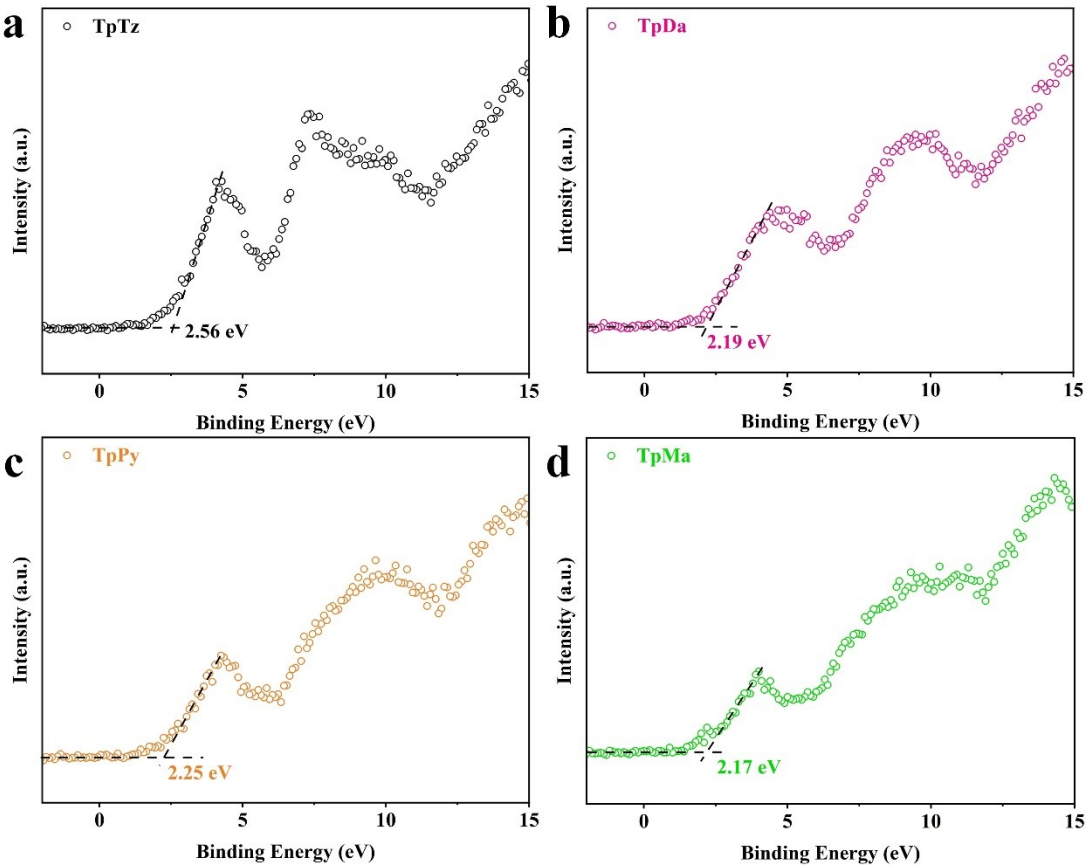

Figure S7. VB-XPS spectra of (a) TpTz, (b) TpDa, (c) TpPy and (d) TpMa.

The valence band maximums (VBM) versus normal hydrogen electrode (NHE) were estimated by the formula $E_{NHE}/V = E + \Phi - 4.5$ (E: electrode potential measured by VB-XPS; Φ of 4.20 eV: the electron work function of the analyzer).

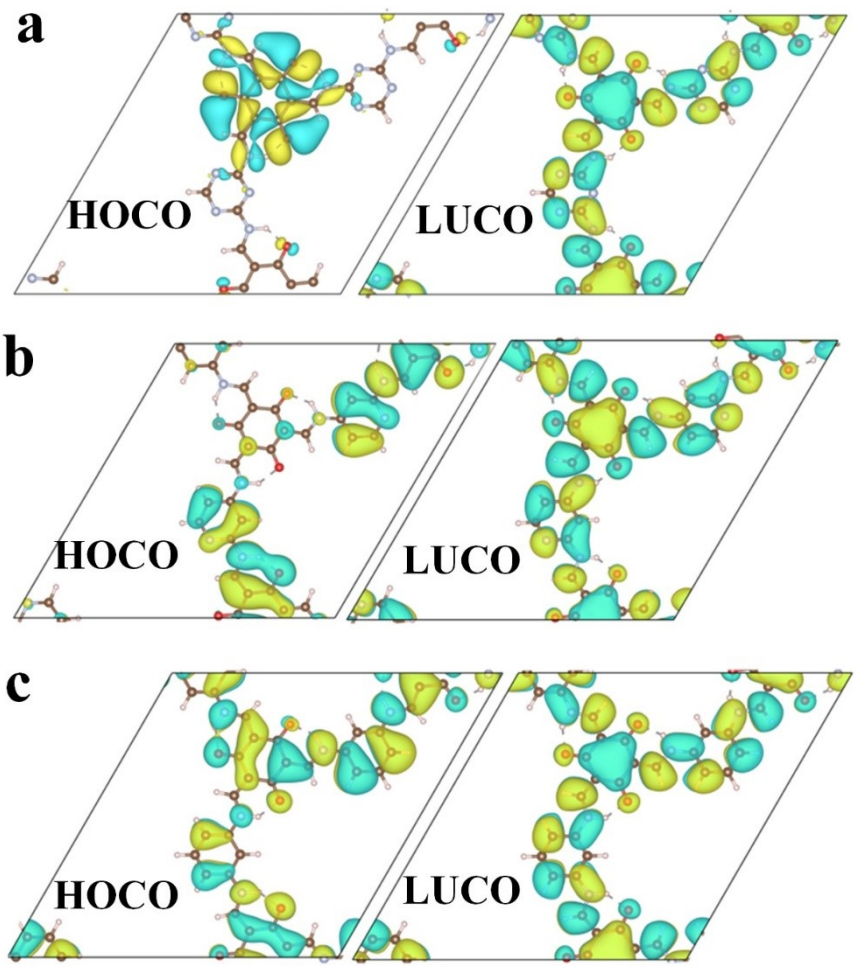

Figure S8. HOCO and LUCO distribution of (a) TpTz, (b)TpPy and (c) TpMa.

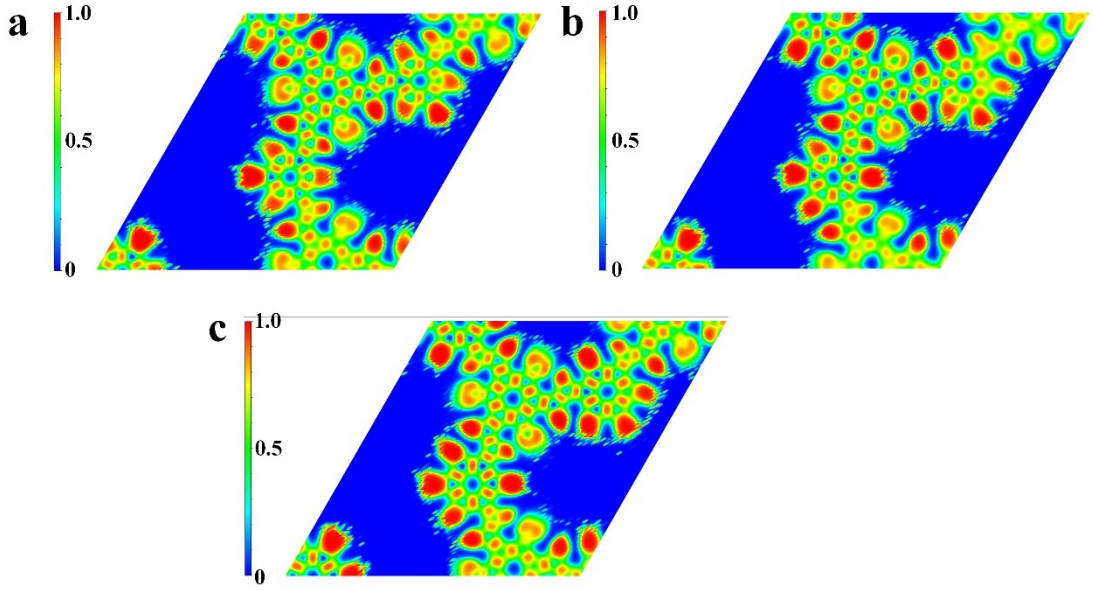

Figure S9. The calculated Electron Localization Function (ELF) diagrams of (a) TpTz, (b) TpPy and (c) TpMa. Red and blue represent complete localization and complete delocalization of electrons, respectively.

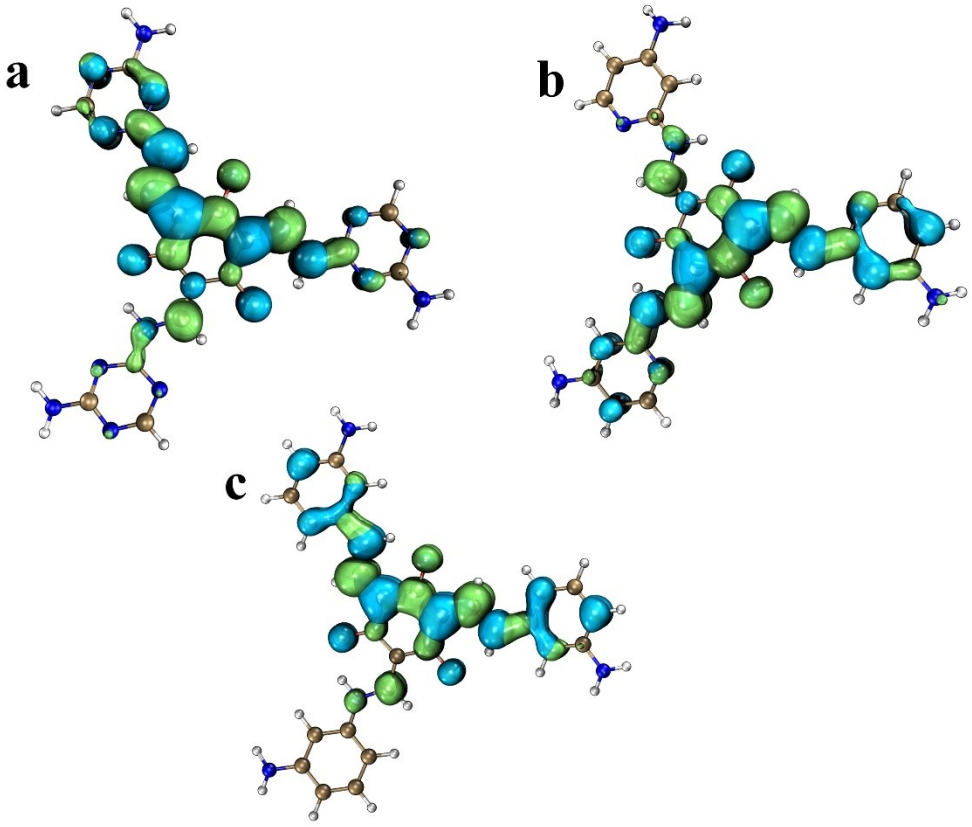

Figure S10. Distribution of holes (blue) and electrons (green) in (a) TpTz, (b)TpPy and (c) TpMa obtained through the time-dependent density functional theory (TD-DFT) calculations (Isosurface value = 0.001).

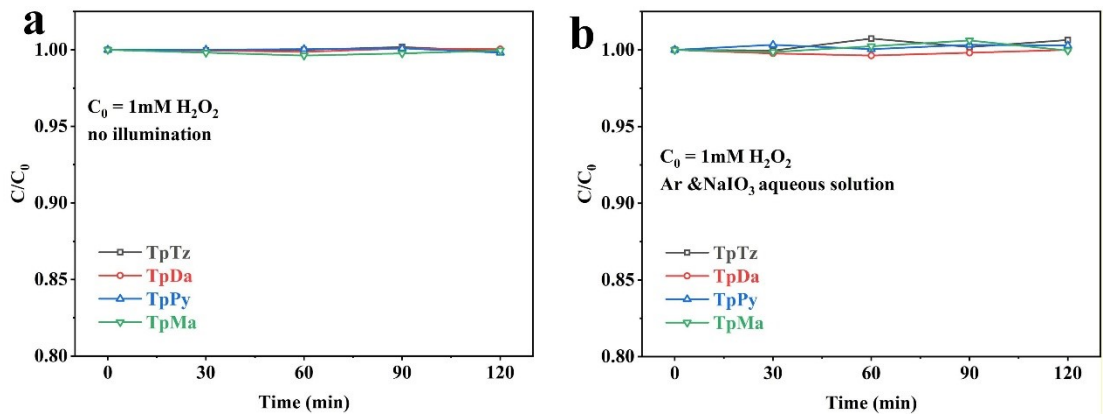

Figure S11. (a) Photocatalytic decomposition of H_2O_2 (C_0 = 1 mM) under dark conditions over COFs. (b) Photocatalytic decomposition of H_2O_2 (C_0 = 1 mM) in $NaIO_3$ aqueous solution (20 mM) under Ar atmosphere over COFs.

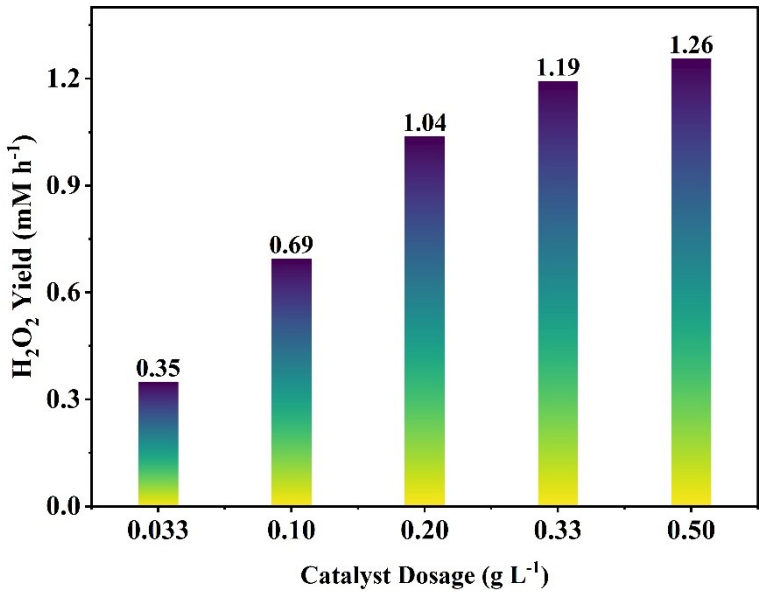

Figure S12. Effects of TpDa dosage on H_2O_2 photosynthesis.

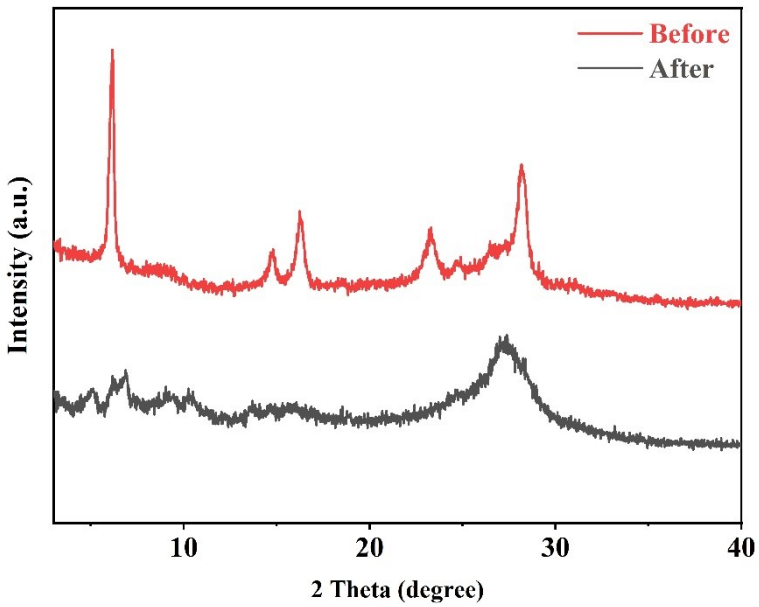

Figure S13. The PXRD patterns of TpDa after undergoing recycling experiments.

As shown in Figure S13, noticeable changes in the PXRD pattern are observed after the photocatalytic reaction. In particular, the characteristic diffraction peaks corresponding to the (100) and (001) planes of TpDa significantly decrease in intensity. The (100) peak reflects the in-plane periodicity of the COF framework, while the (001) peak is associated with the interlayer π–π stacking along the c-axis. The attenuation of these peaks indicates a partial decrease in crystallinity after the photocatalytic process.

This phenomenon can be attributed to structural perturbations induced during the photocatalytic reaction, such as surface reconstruction, adsorption of reaction intermediates, or slight disorder in the interlayer stacking. Such changes can weaken the long-range ordering of the framework, resulting in reduced diffraction intensity. Importantly, the main diffraction features of TpDa are still observable, suggesting that the overall framework structure remains largely preserved after the reaction.

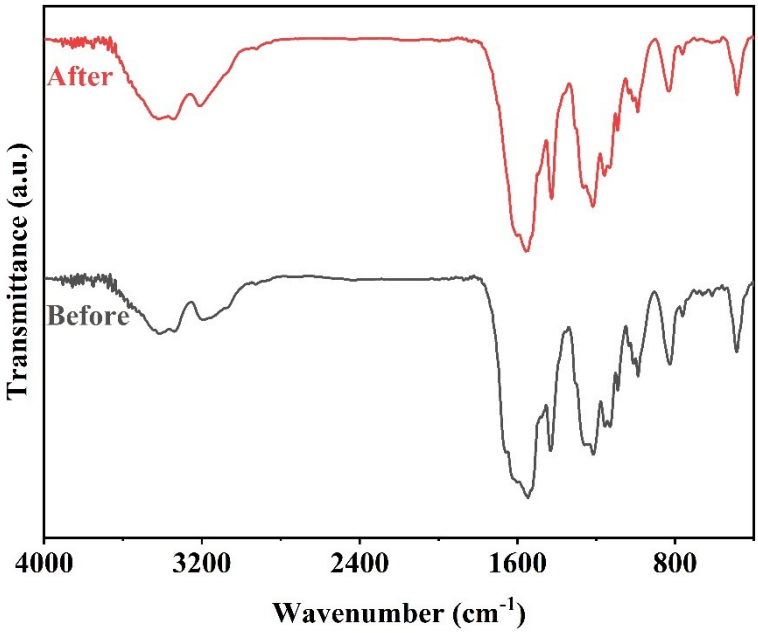

Figure S14. The FT-IR spectra of TpDa after undergoing recycling experiments.

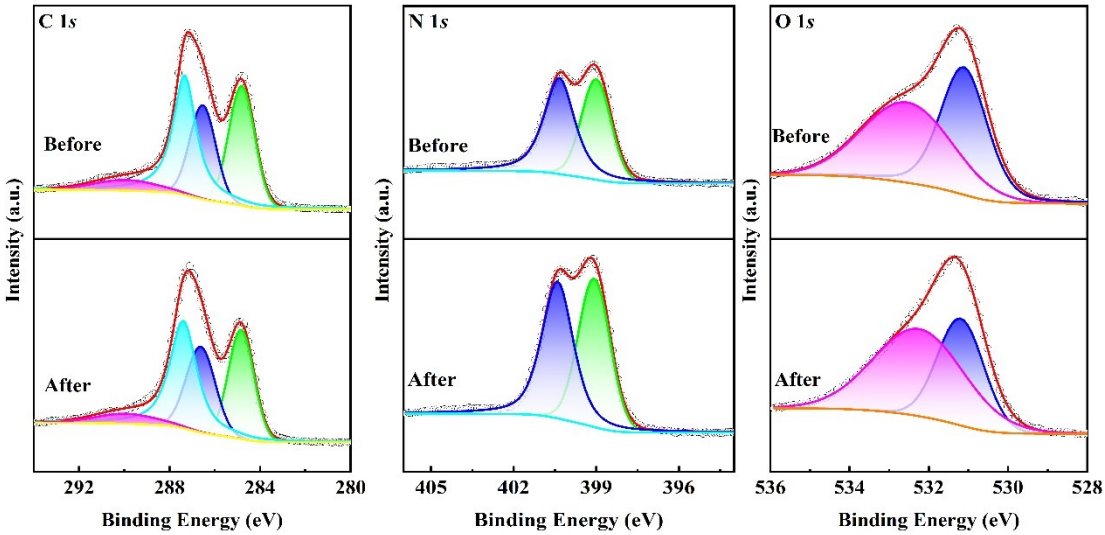

Figure S15. The XPS spectra of TpDa after undergoing recycling experiments.

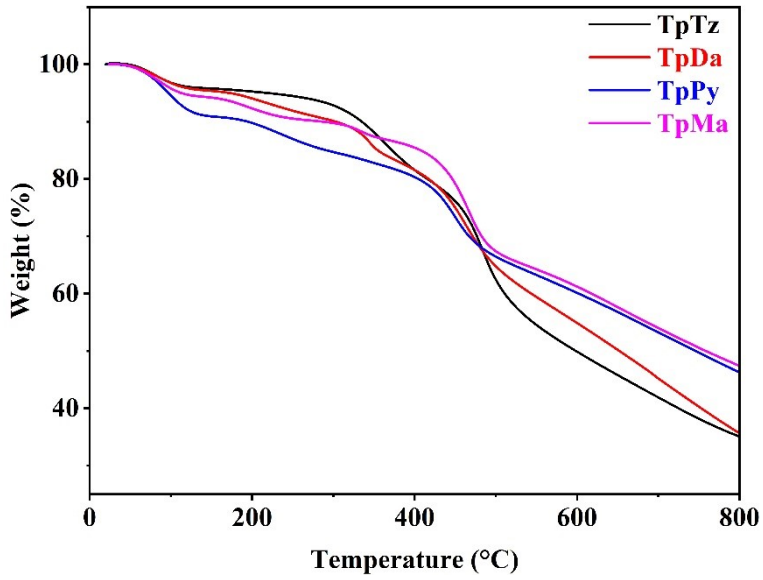

Figure S16. TG plots of COFs.

As shown in Figure S16, the weight loss below 150 °C can be attributed to the desorption of physically adsorbed water or residual solvents. In the temperature range of 200-300 °C, TpPy exhibits a more noticeable weight loss compared with the other COFs.

This behavior should be associated with the relatively lower crystallinity of TpPy and the presence of structurally less ordered regions within the framework. In addition, the pyridine unit introduces local electronic polarization in the framework, which may increase structural strain at edge or defect sites. As a result, these less ordered regions are more susceptible to partial decomposition upon heating around 200 °C.

In contrast, although TpMa exhibits a relatively large surface area, its benzene-based framework lacks heteroatom-induced polarization, resulting in a more uniform electronic environment and slightly higher thermal tolerance of the framework units. Therefore, the observed weight loss of TpPy in the 200-300 °C range is more reasonably attributed to the partial decomposition of less ordered or defect regions rather than the collapse of the entire framework. Significant decomposition of the COF backbones occurs only above 400 °C.

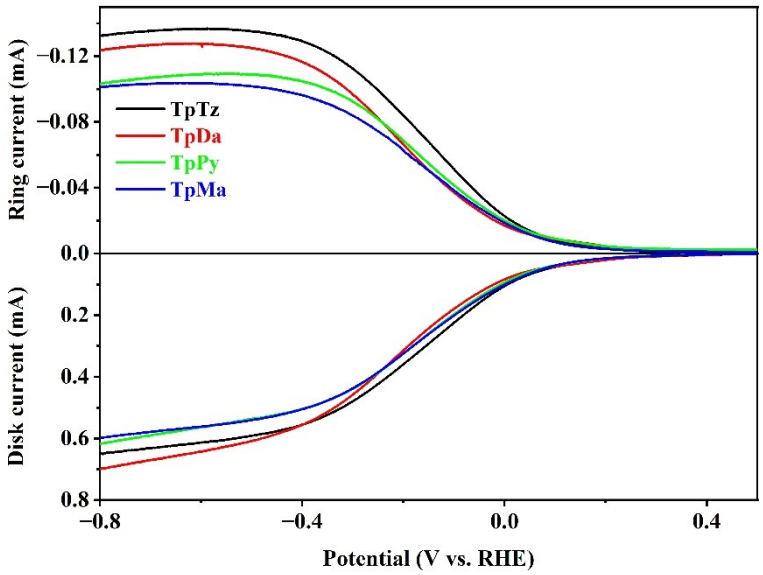

Figure S17. RRDE polarization curves over COFs at 1600 rpm in O_2-saturated phosphate buffer solution (0.1 m pH = 6.9) with ring current (upper part) and disk current (bottom part).

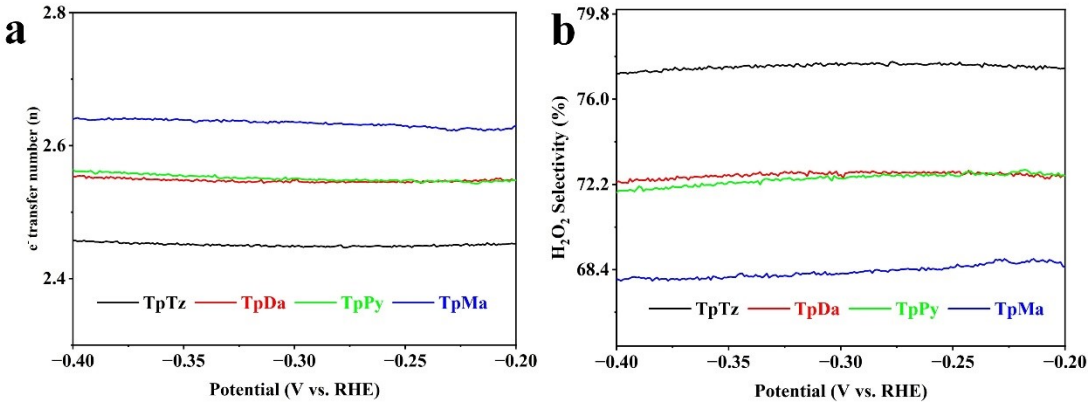

Figure S18. (a) The calculated average number of transferred electrons (n) as a function of the applied potential. (b) H_2O_2 selectivity as a function of the applied potential.

The RRDE measurements were repeated several times to ensure consistency, and the calculated electron transfer numbers and selectivities remained within the same range. The reported values therefore represent consistent trends among the four COFs.

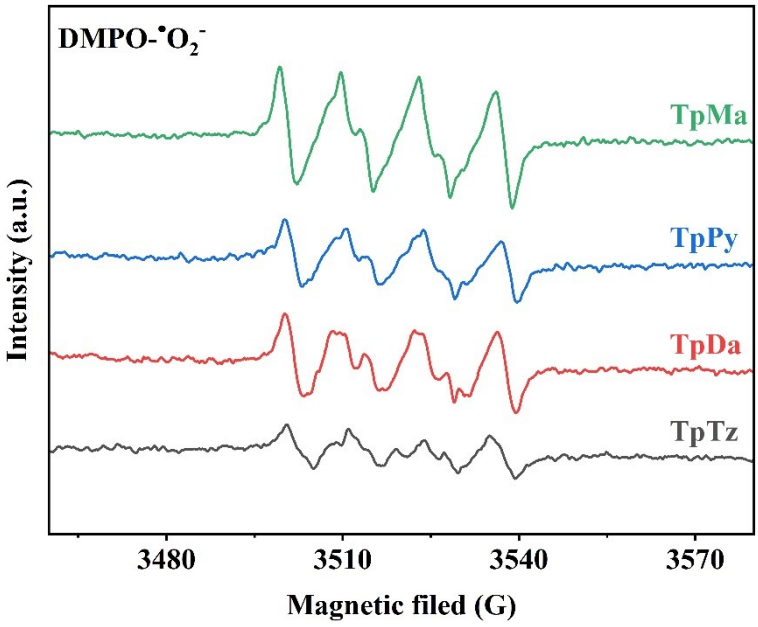

Figure S19. EPR profiles with DMPO for $•O_2^-$ trapping in tBA based on COFs after 5 min irradiation of visible light.

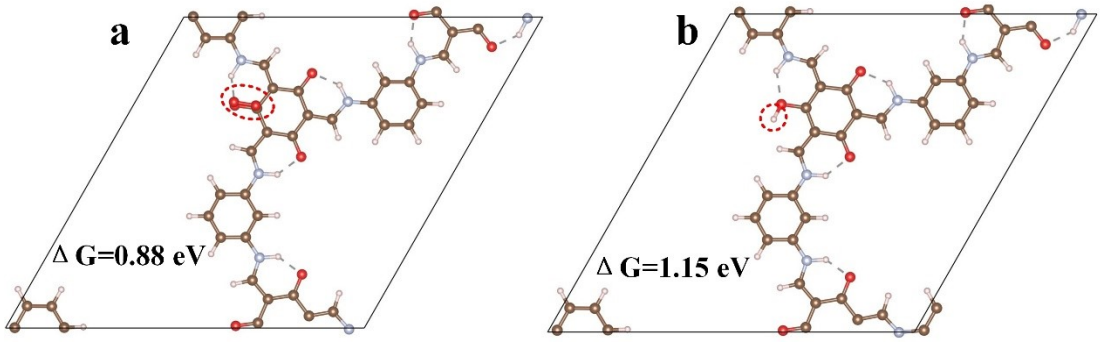

Figure S20. Structure snapshots and calculated reaction free energy of (a) O_2 adsorption and (b) H^+ adsorption on TpMa. Adsorbed species are marked with red dashed circles. The red, blue, white and brown spheres represent the O, N, H and C atoms.

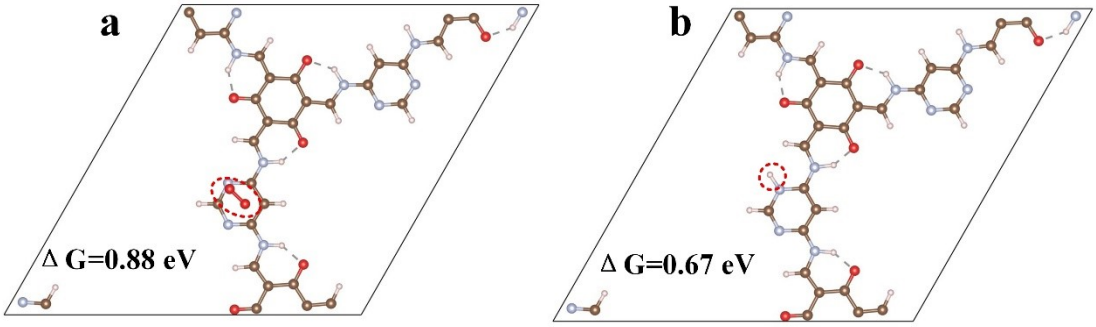

Figure S21. Structure snapshots and calculated reaction free energy of (a) O_2 adsorption and (b) H^+ adsorption on TpDa. Adsorbed species are marked with red dashed circles.

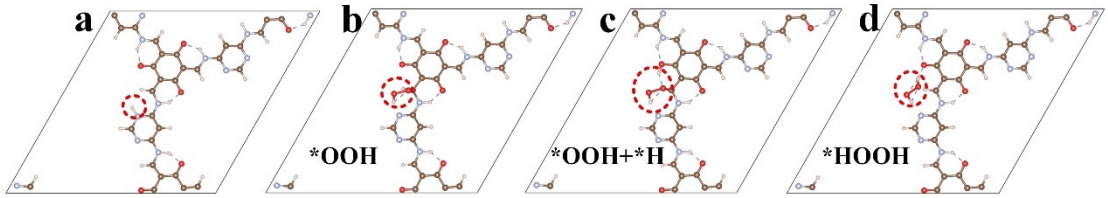

Figure S22. Structural snapshot of key reaction intermediates related $2e^-$ ORR on TpDa. Adsorbed species are marked with red dashed circles.

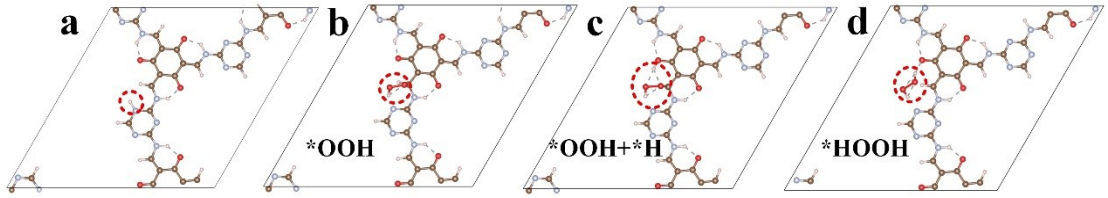

Figure S23. Structure snapshots of key reaction intermediates related $2e^-$ ORR on TpTz. Adsorbed species are marked with red dashed circles.

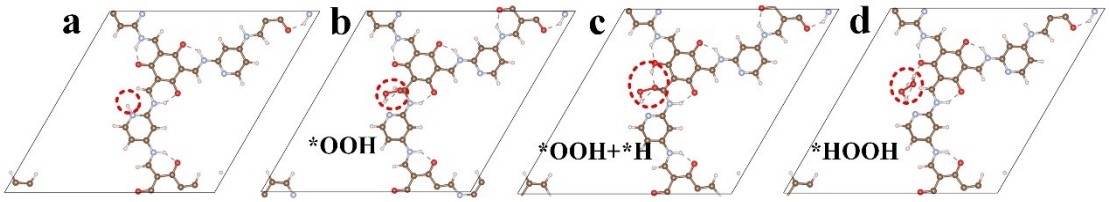

Figure S24. Structure snapshots of key reaction intermediates related $2e^-$ ORR on TpPy. Adsorbed species are marked with red dashed circles.

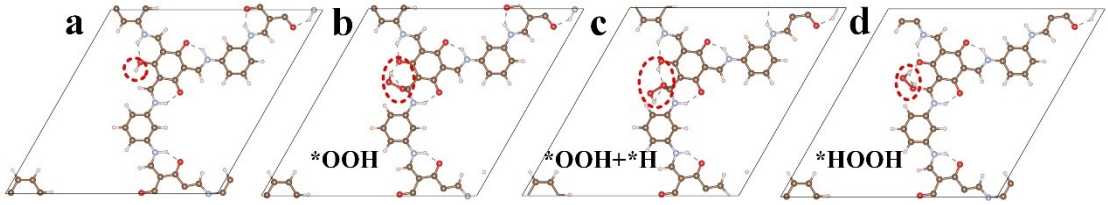

Figure S25. Structure snapshots of key reaction intermediates related $2e^-$ ORR on TpMa. Adsorbed species are marked with red dashed circles.

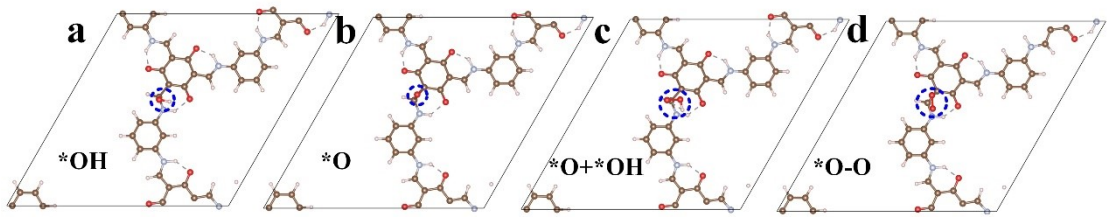

Figure S26. Structural snapshot of the relevant 4e- WOR key reaction intermediate at the site1 (C=C on the ketoenamine chain) of TpMa. Adsorbed species are marked with blue dashed circles.

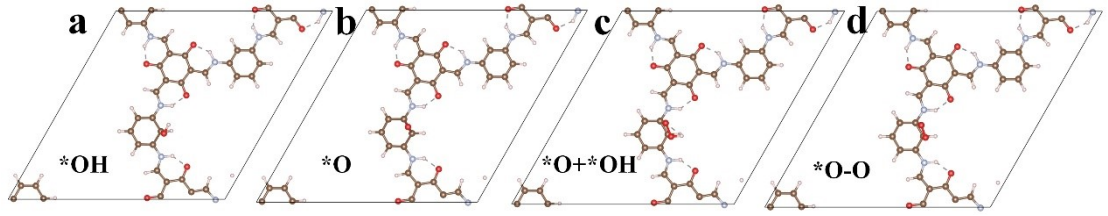

Figure S27. Structural snapshot of the relevant 4e- WOR key reaction intermediate at the site2 (C = C on the aromatic ring) of TpMa. Adsorbed species are marked with blue dashed circles.

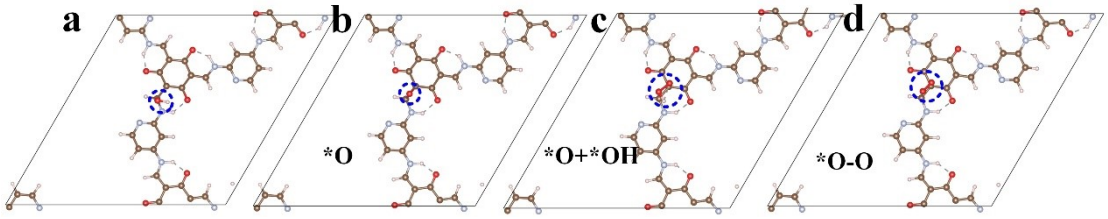

Figure S28. Structural snapshot of the relevant 4e- WOR key reaction intermediate at the site1 (C=C on the ketoenamine chain) of TpPy. Adsorbed species are marked with blue dashed circles.

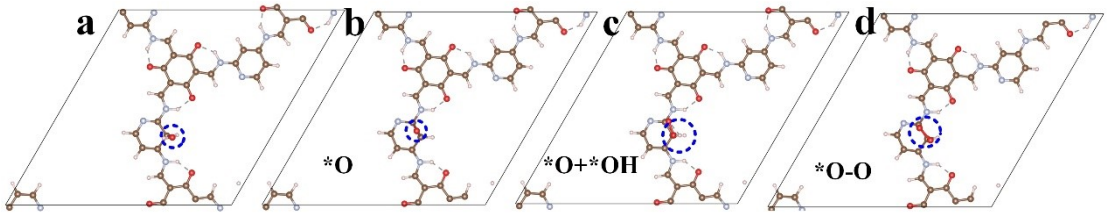

Figure S29. Structural snapshot of the relevant 4e- WOR key reaction intermediate at the site2 (C = C on the aromatic ring) of TpPy. Adsorbed species are marked with blue dashed circles.

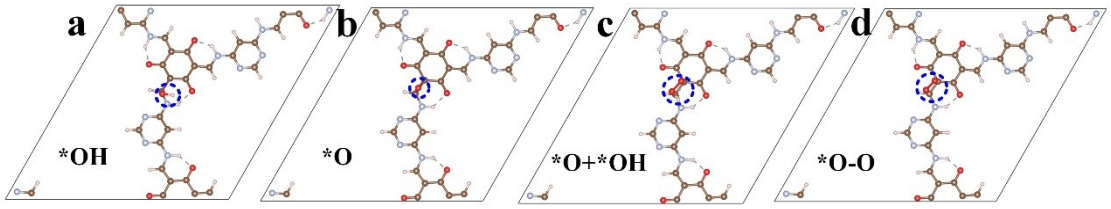

Figure S30. Structural snapshot of the relevant 4e- WOR key reaction intermediate at the site1 (C=C on the ketoenamine chain) of TpDa. Adsorbed species are marked with blue dashed circles.

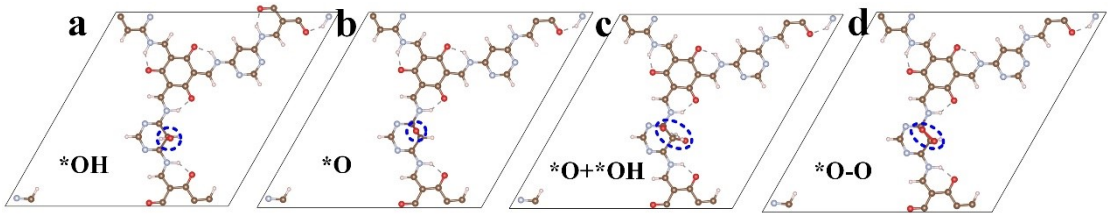

Figure S31. Structural snapshot of the relevant 4e- WOR key reaction intermediate at the site2 (C = C on the aromatic ring) of TpDa. Adsorbed species are marked with blue dashed circles.

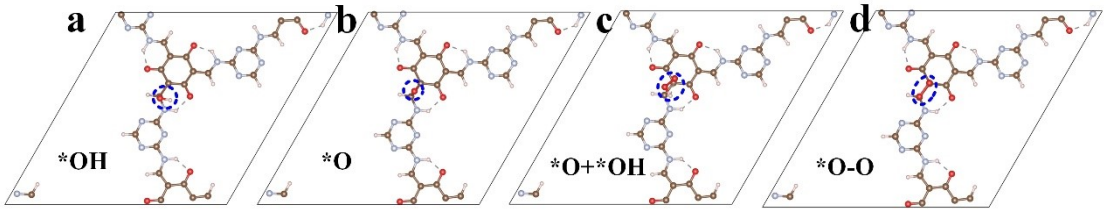

Figure S32. Structural snapshot of the relevant 4e- WOR key reaction intermediate of TpTz. Adsorbed species are marked with blue dashed circles.

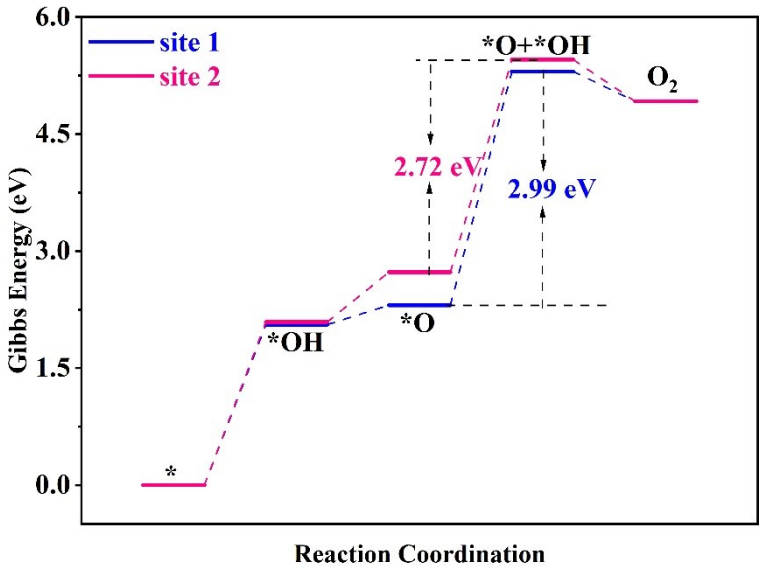

Figure S33. Gibbs free energy diagrams for 4e- WOR at different sites based on TpMa.

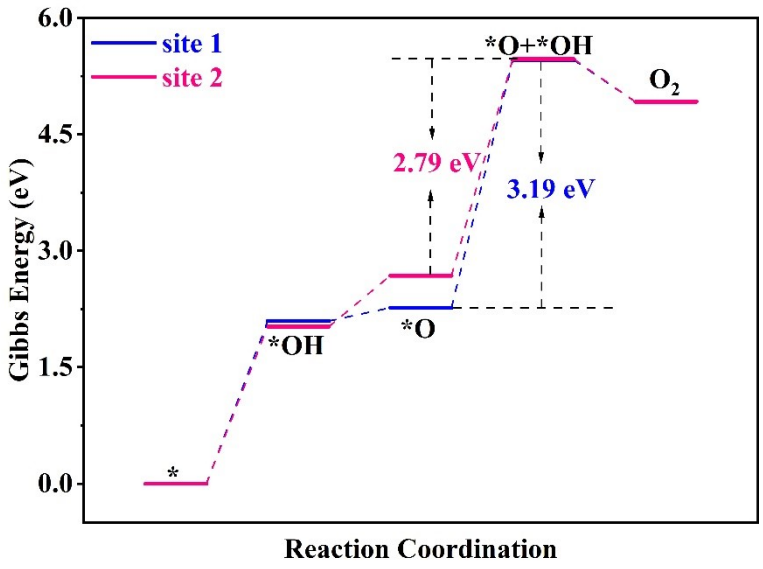

Figure S34. Gibbs free energy diagrams for 4e- WOR at different sites based on TpPy.

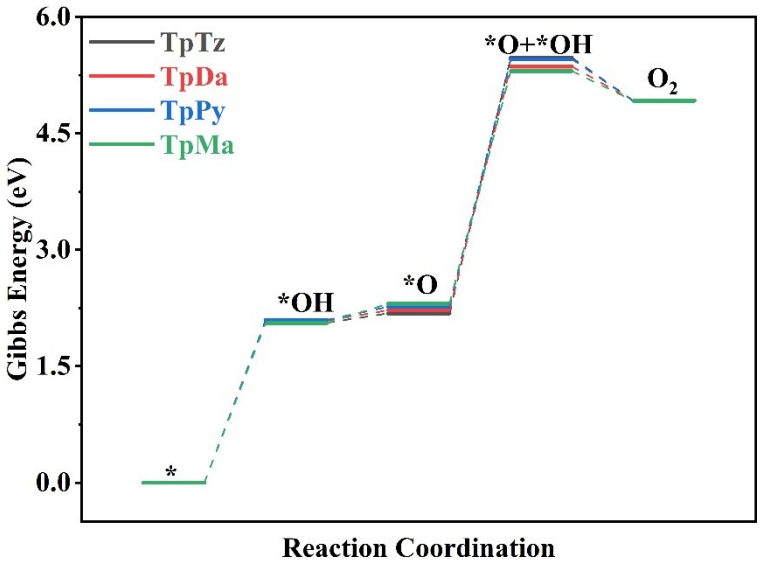

Figure S35. Gibbs free energy diagrams for 4e- WOR at site1 based on four COFs.

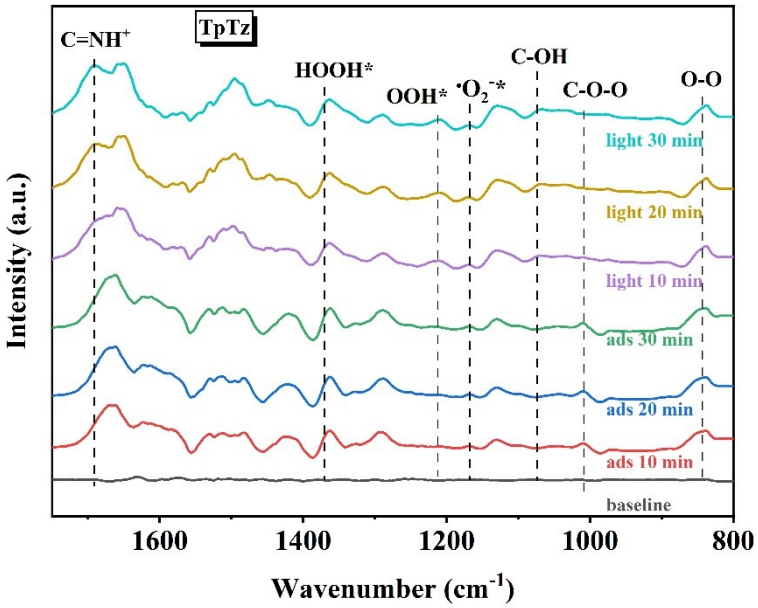

Figure S36. In situ DRIFT spectra of TpTz.

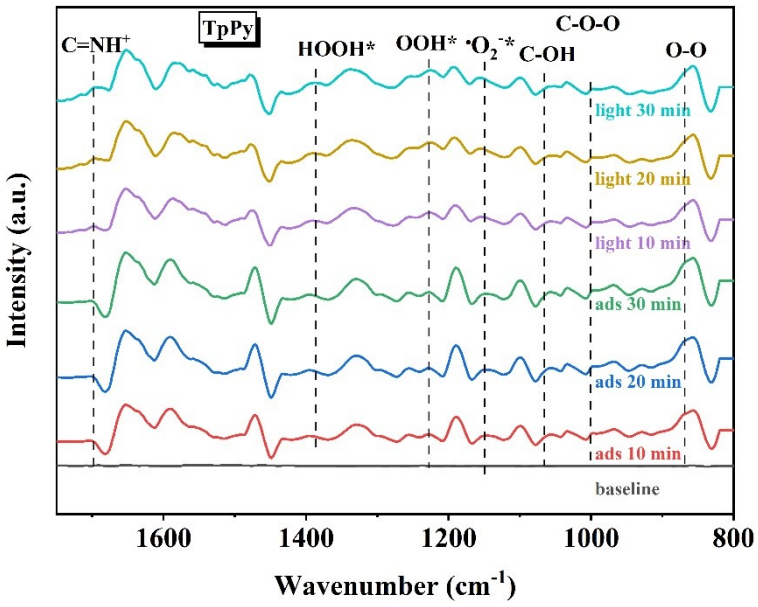

Figure S37. In situ DRIFT spectra of TpPy.

Table S1. Elemental content analysis of COFs obtained by Elemental Analyzer.

	C (wt.%)	N (wt.%)
TpTz	45.11	28.55
TpDa	48.20	24.40
TpPy	52.53	16.28
TpMa	58.88	11.47

Table S2. Elemental content analysis of COFs obtained by XPS.

	C (at.%)	N (at.%)
TpTz	56.35	27.9
TpDa	60.58	20.98
TpPy	66.77	16.63
TpMa	73.42	12.54

Table S3. Fitting parameters of time-resolved PL spectra of COFs.

Samples	A_1	τ_1/ns	A_2	τ_2/ns	τ_n/ns
TpTz	1655.32	0.76	32.40	17.64	6.02
TpDa	1291.32	0.82	64.75	14.96	7.57
TpPy	1481.86	0.40	36.84	5.00	1.93
TpMa	1514.42	0.67	216.83	2.73	1.43

A di-exponential function fitting was employed to analyze the PL decay curves, τ_n is the average PL lifetime, τ_1 and τ_2 are the estimated lifetime values and A_1 and A_2 are the corresponding amplitudes.

$$\tau_n = \frac{A_1 * {\tau_1}^2 + A_2 * {\tau_2}^2}{A_1 * \tau_1 + A_2 * \tau_2}$$

Table S4. The comparison of photocatalytic H_2O_2 production performance of EBBT-COF and PBBT-COF with thus far reported photocatalysts.

Sample	H_2O_2 Yield (mmol g-1 h-1)	Irradiated conditions	AQY (%)	Solvent
TpDa	**7.09**	**Xenon Lamp**	**25.2 (400nm)**	**H_2O**
CQD-CTFs[13]	1.03	λ > 420 nm	1.0 (420 nm)	H_2O
FS-OHOHMe-COF[14]	1.46	λ > 420 nm	9.6 (420 nm)	H_2O:BA (9:1)
SO_3H-COF[15]	3.02	λ > 400 nm	8.7 (400 nm)	H_2O
DVA-COF[16]	3.76	λ > 420 nm	2.8 (420 nm)	H_2O:BA (9:1)
Fe-SAS-TpPP[17]	4.13	AM 1.5	6.4 (420 nm)	H_2O:BA (9:1)
COF-OH[18]	4.46	λ > 400 nm	6.5 (400 nm)	H_2O
KfAQ-COF[19]	4.78	λ > 400 nm	15.8 (400 nm)	Alkaline H_2O
USTB-7–10[20]	5.04	λ > 420 nm	5.0 (420 nm)	H_2O
TBD-COF[21]	5.45	λ > 420 nm	5.7 420 nm)	H_2O
EBBT-COF[22]	5.69	λ > 400 nm	15.1 (420 nm)	H_2O
TAH-COF[23]	6.00	λ > 420 nm	7.1 (475 nm)	H_2O

TPB-COF-OH[24]	6.61	λ > 420 nm	9.6 (420 nm)	H_2O
Tp-$DPBD_{30}$-COF[25]	7.20	λ > 420 nm	18.0 (420 nm)	H_2O
TpDz[26]	7.33	λ > 420 nm	11.9 (420 nm)	H_2O
iTPPy-COF[27]	7.96	λ > 420 nm	8.3 (420 nm)	H_2O
DT2TA-TAPB[28]	8.59	λ > 420 nm	3.3 (380 nm)	H_2O

References

1. H. Zhao, Q. Jin, M. A. Khan, S. Larter, S. Siahrostami, M. G. Kibria and J. Hu, Rational design of carbon nitride for remarkable photocatalytic H_2O_2 production, *Chem Catal.*, 2022, **2**, 1720-1733.
2. C. Feng, J. Luo, C. Chen, S. Zuo, Y. Ren, Z.-P. Wu, M. Hu, S. Ould-Chikh, J. Ruiz-Martínez, Y. Han and H. Zhang, Cooperative tungsten centers in polymeric carbon nitride for efficient overall photosynthesis of hydrogen peroxide, *Energy Environ. Sci.*, 2024, **17**, 1520-1530.
3. Y. Hou, P. Zhou, F. Liu, Y. Lu, H. Tan, Z. Li, M. Tong and J. Ni, Efficient Photosynthesis of Hydrogen Peroxide by Cyano-Containing Covalent Organic Frameworks from Water, Air and Sunlight, *Angew. Chem. Int. Ed.*, 2024, **63**, e202318562.
4. Z. Teng, Q. Zhang, H. Yang, K. Kato, W. Yang, Y.-R. Lu, S. Liu, C. Wang, A. Yamakata, C. Su, B. Liu and T. Ohno, Atomically dispersed antimony on carbon nitride for the artificial photosynthesis of hydrogen peroxide, *Nat. Catal.*, 2021, **4**, 374-384.
5. G. Kresse and J. Hafner, Ab initio molecular dynamics for liquid metals, *Physical review B*, 1993, **47**, 558.
6. G. Kresse and J. Hafner, Ab initio molecular-dynamics simulation of the liquid-metalamorphous-semiconductor transition in germanium, *Physical Review B*, 1994, **49**, 14251-14269.
7. G. Kresse, From ultrasoft pseudopotentials to the projector augmented-wave method, *Physical Review B - Condensed Matter and Materials Physics*, 1999, **59**, 1758-1775.
8. J. P. Perdew, K. Burke and M. Ernzerhof, Generalized gradient approximation made simple, *Phys. Rev. Lett.*, 1996, **77**, 3865.
9. S. Grimme, J. Antony, S. Ehrlich and H. Krieg, A consistent and accurate ab initio parametrization of density functional dispersion correction (DFT-D) for the 94 elements H-Pu, *The Journal of chemical physics*, 2010, **132**, 154104.
10. F. Neese, F. Wennmohs, U. Becker and C. Riplinger, The ORCA quantum chemistry program package, *The Journal of Chemical Physics*, 2020, **152**, 224108.
11. T. Lu, A comprehensive electron wavefunction analysis toolbox for chemists, Multiwfn, *The Journal of Chemical Physics*, 2024, **161**, 082503.
12. W. Humphrey, A. Dalke and K. Schulten, VMD: Visual molecular dynamics, *J. Mol. Graphics*, 1996, **14**, 33-38.
13. Y. Yang, Q. Guo, Q. Li, L. Guo, H. Chu, L. Liao, X. Wang, Z. Li and W. Zhou, Carbon Quantum Dots Confined into Covalent Triazine Frameworks for Efficient Overall Photocatalytic H_2O_2 Production, *Adv. Funct. Mater.*, 2024, **34**, 2400612.
14. C. Shu, X. Yang, L. Liu, X. Hu, R. Sun, X. Yang, A. I. Cooper, B. Tan and X. Wang, Mixed-Linker Strategy for the Construction of Sulfone-Containing D–A–A Covalent Organic Frameworks for Efficient Photocatalytic Hydrogen Peroxide Production, *Angew. Chem. Int. Ed.*, 2024, **63**, e202403926.
15. L. Li, X. Lv, Y. Xue, H. Shao, G. Zheng and Q. Han, Custom-Design of Strong Electron/Proton Extractor on COFs for Efficient Photocatalytic H_2O_2 Production, *Angew. Chem. Int. Ed.*, 2024, **63**, e202320218.
16. H. Yu, F. Zhang, Q. Chen, P.-K. Zhou, W. Xing, S. Wang, G. Zhang, Y. Jiang and X. Chen, Vinyl-Group-Anchored Covalent Organic Framework for Promoting the Photocatalytic Generation of Hydrogen Peroxide, *Angew. Chem. Int. Ed.*, 2024, **63**, e202402297.
17. Z. Li, X. Shi, H. Cheng, Y. Song, Y. Jiao, S. Shi, J. Gao and J. Hou, Atomically Dispersed Iron Active Sites on Covalent Organic Frameworks for Artificial Photosynthesis of Hydrogen Peroxide, *Adv. Energy Mater.*, 2024, **14**, 2302797.
18. M. Guo, C. He, Z. Wu, Y. Tian, J. Yang, Y. Wang, H. Wu, J. Yang, M. Xu, W. Xue, C. Cheng, S. Li and C.

Zhao, Micro-Environment Programmable Quinoline COFs for High-Performance Photocatalytic H_2O_2 Generation and Benzylamine Coupling, *Adv. Sci.*, 2025, **12**, e05794.

19. X. Zhang, S. Cheng, C. Chen, X. Wen, J. Miao, B. Zhou, M. Long and L. Zhang, Keto-anthraquinone covalent organic framework for H_2O_2 photosynthesis with oxygen and alkaline water, *Nat. Commun.*, 2024, **15**, 2649.
20. X. Ding, T. Wang, B. Yu, Q. Zhi, H. Wang, H. Liu, P. A. Stuzhin and J. Jiang, 10% Conversion of Imine into Thiazole in Covalent Organic Frameworks for Efficient Photocatalytic H_2O_2 Generation, *Adv. Funct. Mater.*, 2025, **35**, 2422291.
21. J.-Y. Yue, J.-X. Luo, Z.-X. Pan, R.-Z. Zhang, P. Yang, Q. Xu and B. Tang, Regulating the Topology of Covalent Organic Frameworks for Boosting Overall H_2O_2 Photogeneration, *Angew. Chem. Int. Ed.*, 2024, **63**, e202405763.
22. B. Li, J. Chen, K. Wang, D. Qi, T. Wang and J. Jiang, Ethynyl-Linked Donor–Acceptor Covalent Organic Framework for Highly Efficient Photocatalytic H_2O_2 Production, *Adv. Energy Mater.*, 2025, **15**, 2404497.
23. T. Xu, Z. Wang, W. Zhang, S. An, L. Wei, S. Guo, Y. Huang, S. Jiang, M. Zhu, Y.-B. Zhang and W.-H. Zhu, Constructing Photocatalytic Covalent Organic Frameworks with Aliphatic Linkers, *Journal of the American Chemical Society*, 2024, **146**, 20107-20115.
24. S. Feng, H. Cheng, F. Chen, X. Liu, Z. Wang, H. Xu and J. Hua, Rational Design of Covalent Organic Frameworks with Redox-Active Catechol Moieties for High-Performance Overall Photosynthesis of Hydrogen Peroxide, *ACS Catal.*, 2024, **14**, 7736-7745.
25. Y. Chen, R. Liu, Y. Guo, G. Wu, T. C. Sum, S. W. Yang and D. Jiang, Hierarchical assembly of donor–acceptor covalent organic frameworks for photosynthesis of hydrogen peroxide from water and air, *Nat. Synth.*, 2024, **3**, 998-1010.
26. Q. Liao, Q. Sun, H. Xu, Y. Wang, Y. Xu, Z. Li, J. Hu, D. Wang, H. Li and K. Xi, Regulating Relative Nitrogen Locations of Diazine Functionalized Covalent Organic Frameworks for Overall H_2O_2 Photosynthesis, *Angew. Chem. Int. Ed.*, 2023, **62**, e202310556.
27. J. Zhang, F. Xue and Z. Wang, Terpyridine- and Quarterpyridine-Based Cationic Covalent Organic Frameworks for Visible-Light-Catalytic H_2O_2 Synthesis, *Angew. Chem. Int. Ed.*, 2025, **64**, e202425617.
28. Y. Ju, H. Lin, G. Tan, P. Su, Z. Wang, C. Hu, R. Hou, T. Hao, F. Chen and Y. Tang, Regulating the electronic structure of covalent organic frameworks via heterocyclic isomers for highly efficient photocatalytic H_2O_2 generation, *Nat. Commun.*, 2025, **16**, 5658.